

Rotation of Halo Populations in the Milky Way and M31

A.J. Deason^{1*}, V. Belokurov¹ and N. W. Evans¹

¹*Institute of Astronomy, Madingley Rd, Cambridge, CB3 0HA*

Accepted 2010 September 28. Received 2010 September 27; in original form 2010 May 05

ABSTRACT

We search for signs of rotation in the subsystems of the Milky Way and M31 that are defined by their satellite galaxies, their globular cluster populations, and their BHB stars. A set of simple distribution functions are introduced to describe anisotropic and rotating stellar populations embedded in dark haloes of approximate Navarro-Frenk-White form. The BHB stars in the Milky Way halo exhibit a dichotomy between a prograde rotating, comparatively metal-rich component ($[\text{Fe}/\text{H}] > -2$) and a retrograde rotating, comparatively metal-poor ($[\text{Fe}/\text{H}] < -2$) component. The prograde metal-rich population may be associated with the accretion of a massive satellite ($\sim 10^9 M_\odot$). The metal-poor population may characterise the primordial stellar halo and the net retrograde rotation could then reflect an underestimate in our adopted local standard of rest circular velocity Θ_0 . If Θ_0 is $\approx 240 \text{ km s}^{-1}$ then the metal-poor component has no rotation and there is a net prograde rotation signal of $\approx 45 \text{ km s}^{-1}$ in the metal-rich component. There is reasonable evidence that the Milky Way globular cluster and satellite galaxy systems are rotating with $\langle v_\phi \rangle \approx 50 \text{ km s}^{-1}$ and $\langle v_\phi \rangle \approx 40 \text{ km s}^{-1}$ respectively. Furthermore, a stronger signal is found for the satellite galaxies when the angular momentum vector of the satellites is inclined with respect to the normal of the disc. The dwarf spheroidal satellites of M31 exhibit prograde rotation relative to the M31 disc with $\langle v_\phi \rangle \approx 40 \text{ km s}^{-1}$. We postulate that this group of dwarf spheroidals may share a common origin. We also find strong evidence for systemic rotation in the globular clusters of M31 particularly for the most metal-rich.

Key words: galaxies: general – galaxies: haloes – galaxies: kinematics and dynamics – galaxies: individual: M31 – dark matter

1 INTRODUCTION

Our own Milky Way Galaxy and its nearest neighbour Andromeda (M31) provide testing grounds for theories of galaxy formation and evolution. Studies of local stellar populations explore the complex processes which built up the galaxies. The orbits of tracer populations bear the imprint of the infall and subsequent accretion history of the dark matter halo. In a monolithic collapse model (see e.g., Eggen et al. 1962), the halo and the disc of the galaxy are drawn from the same population. Any rotational signature in the outer halo is thus aligned with the angular momentum of the disc. However, in a hierarchical picture, substructure arriving late at large radii may have little connection to the disc. Its evolution is further complicated by processes such as tidal disruption, disk shocking and dynamical friction. For example, prograde rotating systems are more susceptible to dynamical friction than retrograde (Quinn & Goodman 1986). Norris & Ryan (1989) suggested that the subsequent disintegration of these accreted fragments by tidal forces may create a net retrograde asymmetry in the remnant stellar halo population. The presence, or absence, of a rotating signal can provide key insights into the formation history of the halo.

There have been a number of previous kinematic studies of halo populations in the Milky Way Galaxy. For example, Frenk & White (1980) found that the globular cluster system has a velocity distribution that is isotropic about a net prograde rotation ($v_{\text{rot}} \sim 60 \text{ km s}^{-1}$). Zinn (1985) extended this work by restricting attention to halo globular clusters with $[\text{Fe}/\text{H}] < -1$ and found a slightly weaker net prograde motion ($v_{\text{rot}} \sim 50 \text{ km s}^{-1}$). Norris (1986) used a sample of metal-poor objects ($[\text{Fe}/\text{H}] < -1.2$) and found evidence for weak prograde rotation, although he found no kinematic difference between the clusters and halo stars, suggesting these are part of the same population.

The isotropic velocity distribution of the globular clusters contrasts with the highly anisotropic distributions usually found for Population II stars (Woolley 1978; Hartwick 1983; Ratnatunga & Freeman 1985). Cosmological simulations generally predict increasing radial anisotropy with Galactocentric radii for halo stars (e.g. Abadi et al. 2006), as a consequence of the accretion of infalling structure. Observationally, the situation is less clear-cut with radially biased (e.g. Chiba & Beers 2000), isotropic (e.g. Sirko et al. 2004b) and even tangentially biased (Sommer-Larsen et al. 1997) velocity distributions claimed for the outer stellar halo.

More recently, a number of authors have advocated a dual

* E-mail: ajd75,vasily,nwe@ast.cam.ac.uk

halo structure, which suggests that the stellar halo was formed by at least two distinct phases of accretion events. The evidence includes studies of the spatial profiles (Hartwick 1987; Kinman et al. 1994; Miceli et al. 2008), as well as kinematic studies indicating net retrograde rotation in the outer parts (Majewski 1992; Carney et al. 1996; Wilhelm et al. 1996; Kinman et al. 2007). For example, Carollo et al. (2007) claimed a dual halo structure consisting of a weakly prograde rotating inner halo and a retrograde rotating outer halo of lower metallicity ($[\text{Fe}/\text{H}] < -2$). However, this idea is inconsistent with work by Chiba & Beers (2000) on local neighbourhood stars and by Sirko et al. (2004b) on distant BHB stars who both find no evidence for rotation in the outer halo.

This somewhat confused picture is partly caused by the difficulties of the task. Full kinematic analyses of tracer populations are hampered by small sample sizes and lack of full information on the phase space coordinates. Often, work has been confined to comparatively local samples, which may not be unbiased tracers of the overall population. This, though, is beginning to change with more recent studies on BHB stars reaching out to distances of ~ 80 kpc (e.g. Sirko et al. 2004b; Xue et al. 2008), albeit with only the line-of-sight velocity available. In fact, several surveys have the promise to provide much larger samples of halo tracers with well-defined kinematical parameters. This includes ongoing projects like the Sloan Digital Sky Survey (SDSS, York et al. 2000), and the Sloan Extension for Galactic Understanding and Exploration (SEGUE, Newberg & Sloan Digital Sky Survey Collaboration 2003), as well as future projects like the *Gaia* satellite (Turon et al. 2005), and the Large Synoptic Survey Telescope (LSST, Ivezić et al. 2008).

There has also been a lively debate in recent years as to the possibility that the satellite galaxies of the Milky Way lie in a rotationally-supported disc. The idea may be traced back to Lynden-Bell (1983), who first suggested the Magellanic Clouds, Ursa Minor and Draco may have been torn from a single progenitor, a gigantic gas-rich proto-Magellanic Cloud. Working with more complete datasets, Kroupa et al. (2005) claimed that satellite galaxies occupy a highly inclined disc and that this is at odds with the predictions of cosmological simulations. The available proper motion measurements have been used to constrain the angular momenta orientations of the satellites (e.g. Palma et al. 2002; Metz et al. 2008), indicating evidence for some sort of coherent motion, possibly rotation. Even if true, it remains disputatious as to whether this can be reconciled within the cold dark matter framework of structure formation (Metz et al. 2008; Libeskind et al. 2009).

Rotational properties of halo populations can therefore provide clues as to their origin and evolution, and may allow us to identify associations sharing a common formation history. With this in mind, we develop some simple and flexible distribution functions that can model rotating stellar populations embedded in dark halos. Cosmological arguments suggest that dark halos have a universal Navarro-Frenk-White form (Navarro et al. 1996), whilst many stellar populations in the outer halo are well-approximated by a power-law. Section 2 provides a flexible set of simple distribution functions that are powers of energy E and angular momentum L and which can be adapted to include rotation. We apply the models to the satellite galaxy, globular cluster and BHB populations of the Milky Way (Section 3) and M31 (Section 5), with the implications of our results for the Milky Way given particular attention in Section 4. Finally, Section 6 sums up.

2 DISTRIBUTION FUNCTIONS

2.1 The Even Part of the Distribution Function

A collisionless system can be described by a phase-space distribution function (henceforth DF), F . The probability that a star occupies the phase space volume $d^3x d^3v$ is given by $F(x, v)d^3x d^3v$. DFs are a valuable tool for studying steady-state systems as they replace the impracticality of following individual orbits with a phase-space probability density function. The part of the DF that is even in v_ϕ fixes the density, whilst the part that is odd in v_ϕ fixes the rotational properties.

To construct the DFs, we assume a steady-state spherical potential and a density profile for our halo populations. Of course, these are tracer populations moving in an external gravitational field generated by the dark matter halo rather than the self-consistent density generated through Poisson's equation. For simplicity, we use simple power-law profiles for the density and potential, namely $\rho \propto r^{-\alpha}$ and $\Phi \propto r^{-\gamma}$, where α and γ are constants.

The density profiles of dark matter halos in cosmological simulations resemble the Navarro-Frenk-White or NFW profile (Navarro et al. 1996). Exterior to $r \approx 20$ kpc, we can approximate the NFW potential by a power-law profile, as shown in Fig. 1. Here, we have used one of the NFW models applicable to the Milky Way from Klypin et al. (2002), and have normalised the power-law profile to reproduce the local escape speed found by Smith et al. (2007). We see that a power-law with index $\gamma = 0.5$ is a good approximation at large radii ($r > 20$ kpc). At small radii, the approximation breaks down, but in this regime, the bulge and disk components become important. In any case, our main application is to tracer populations that reside far out in the halo. The dark halo mass within a given radius is

$$M(< r) = \frac{\Phi_0 R_\odot^{1/2}}{2G} r^{1/2} \quad (1)$$

where Φ_0 is the normalisation at the solar radius R_\odot . For a virial radius of 250 kpc, the halo mass enclosed is $\approx 8 \times 10^{11} M_\odot$, in good agreement with estimates for the Milky Way Galaxy and M31 (e.g. Evans & Wilkinson 2000; Xue et al. 2008; Battaglia et al. 2005; Watkins et al. 2010).

Previous authors have adopted power-law density profiles for halo populations with $2 < \alpha < 5$. For example, Harris (1976), Zinn (1985) and Djorgovski & Meylan (1994) find a power-law with $\alpha = 3.5$ is a good fit to the Milky Way globular cluster populations. Classical studies have found $\alpha = 3.5$ for stellar populations in the Milky Way halo (e.g. Freeman 1987). More recently, Bell et al. (2008) find values of α in the range $2 - 4$, although they caution against the use of a single power-law due to the abundant substructure in the stellar halo. The density profile of the system of Milky Way satellite galaxies is poorly known due to the small sample size and incompleteness at large radii. Evans & Wilkinson (2001) find $\alpha = 3.4$ is a good approximation for $r > 20$ kpc whilst Watkins et al. (2010) adopt a power law of $\alpha = 2.6$. Similar profiles have been used for the M31 halo populations. Crampton et al. (1985) argue that the radial profile of the M31 globular cluster system is similar to that of the Milky Way and so it is reasonable to adopt the same power-law. Evans & Wilkinson (2000) and Watkins et al. (2010) use α values of 3.5 and 2.1 respectively, for the M31 satellites. As a convenient summary of all this work, we will use a density power-law index of $\alpha = 3.5$, but we discuss the effects of varying α in Section 3.

Armed with these simple forms for the potential and density, we can give the velocity distribution in terms of the binding energy

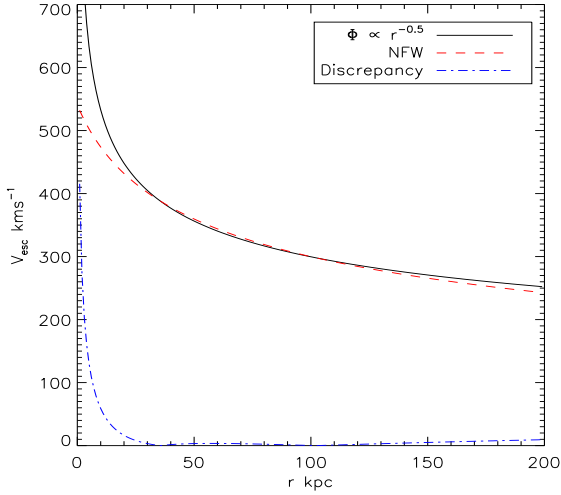


Figure 1. V_{esc} as a function of radius. The power law approximation deviates from a NFW profile at $r < 20$ kpc. The NFW parameters applicable to the Milky Way were taken from Klypin et al. (2002). The normalisation of the power law is chosen to match the local escape velocity derived in Smith et al. (2007).

$E = \Phi(r) - \frac{1}{2}(v_l^2 + v_b^2 + v_{\text{los}}^2)$ and the total angular momentum $L = \sqrt{L_x^2 + L_y^2 + L_z^2}$ as

$$F_{\text{even}}(E, L) \propto L^{-2\beta} f(E) \quad (2)$$

where

$$f(E) = E^{\frac{\beta(\gamma-2)}{\gamma} + \frac{\alpha}{\gamma} - \frac{3}{2}} \quad (3)$$

Here, β is the Binney anisotropy parameter (Binney & Tremaine 1987), namely

$$\beta = 1 - \frac{\langle v_\theta^2 \rangle + \langle v_\phi^2 \rangle}{2\langle v_r^2 \rangle}, \quad (4)$$

which is constant for the DFs of the form of eqn (2). These DFs are discussed in greater detail in Evans et al. (1997).

2.2 The Odd Part of the Distribution Function

So far, our DFs describe non-rotating populations embedded in dark halos. We now devise an odd part to the distribution function which generates a one-parameter family of rotating models

$$F_{\text{odd}} = (1 - \eta)\tanh(L_z/\Delta)F_{\text{even}} \quad (5)$$

where η is a constant. The case $\eta = 0$ describes maximum prograde rotation, whilst $\eta = 2$ describes maximum retrograde rotation. Here, Δ is a ‘smoothing’ parameter to ease numerical calculations and soften the Heaviside function.

To illustrate the effects of the parameter η , we compute the mean streaming velocity $\langle v_\phi \rangle$, which is analytic for $\gamma = 0.5$

$$\langle v_\phi \rangle = \frac{2^{\frac{3}{2}}\Gamma(\frac{3}{2} - \beta)\Gamma(2\alpha - 4\beta + 1)}{\pi\Gamma(1 - \beta)\Gamma(2\alpha - 4\beta + \frac{3}{2})}(1 - \eta)\Phi(r)^{\frac{1}{2}}. \quad (6)$$

Table 1 lists $\langle v_\phi \rangle$ values at $r = 50, 100$ kpc for three different anisotropy parameters. Fig. 2 shows the radial profile of the streaming motion for maximum prograde (solid line) and maximum retrograde (dotted line) distributions.

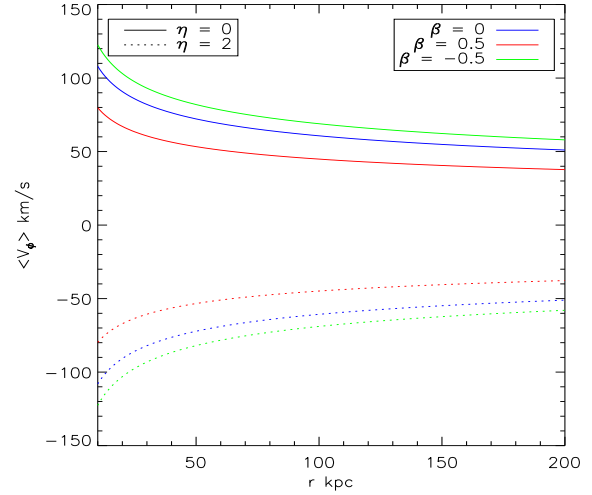


Figure 2. The mean streaming velocity $\langle v_\phi \rangle$ as a function of Galactocentric distance for $\gamma = 0.5$ and $\alpha = 3.5$. Solid and dotted lines correspond to maximum prograde and retrograde rotation respectively. The profile flattens at large radii. Blue, red and green lines represent isotropic, radial and tangential velocity distributions respectively.

η	β	$\langle v_{\phi,50 \text{ kpc}} \rangle \text{ km s}^{-1}$	$\langle v_{\phi,100 \text{ kpc}} \rangle \text{ km s}^{-1}$
0.0	(-0.5, 0, 0.5)	(82, 72, 53)	(69, 61, 45)
0.5	(-0.5, 0, 0.5)	(41, 36, 27)	(34, 30, 22)
1.0	(-0.5, 0, 0.5)	(0, 0, 0)	(0, 0, 0)
1.5	(-0.5, 0, 0.5)	(-41, -36, -27)	(-34, -30, -22)
2.0	(-0.5, 0, 0.5)	(-82, -72, -53)	(-69, -61, -45)

Table 1. Typical $\langle v_\phi \rangle$ values evaluated at $r = 50$ kpc and $r = 100$ kpc as a function of the rotating parameter η and the anisotropy parameter β . [$\gamma = 0.5, \alpha = 3.5$]

2.3 Properties

It is rare that we possess full six-dimensional phase space information for any star. However, we can still use a DF by marginalising over the unknown components. For example, consider a case where the spatial position and line of sight velocity are well known, but the proper motions are uncertain. In this case, we marginalise over v_l and v_b to obtain the line of sight velocity distribution (LOSVD):

$$F(l, b, d, v_{\text{los}}) = \int \int F(l, b, d, v_l, v_b, v_{\text{los}}) dv_l dv_b. \quad (7)$$

Once γ is fixed as 0.5, there remain the free parameters, β , α and η .

Some properties of the distribution functions are shown in Fig. 3. The top left panel shows $F(l, b, d, v_{\text{los}})$ as a function of v_{los} at three different distances from the Sun (for the case $\alpha = 3.5$). An arbitrary line of sight toward the Leo constellation is chosen for illustration, $(l, b) = (230^\circ, 50^\circ)$. Closer to the Galactic Centre the escape velocity is larger, so the velocity distributions are broader. Tangential orbits ($\beta < 0$) have narrower radial velocity and broader tangential velocity distributions. The reverse is true for radial orbits ($\beta > 0$).

For distant objects in the Milky Way, $v_{\text{los}} \approx v_r$ and so the line of sight velocity distribution reflects the radial distribution. At small radii, the trend is not so simple and depends on the particular

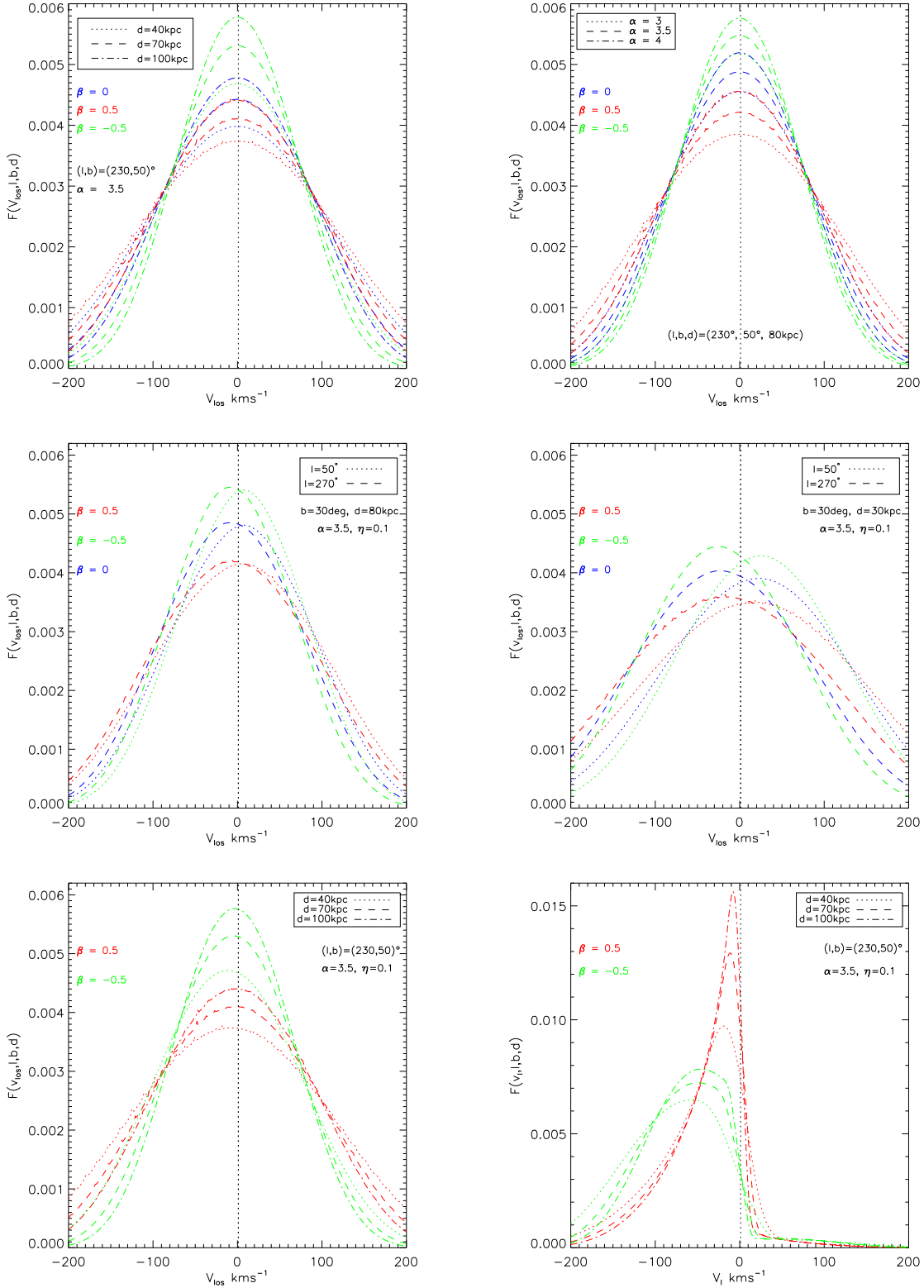


Figure 3. Top left: The dependence of the distribution function on v_{los} at three different distances in the non-rotating case. A random line of sight is chosen (toward the Leo constellation) and the density power law is set to $\alpha = 3.5$. Blue, red and green lines represent isotropic, radial and tangential velocity distributions respectively. Top right: The distribution function for three different density profile power laws in the non-rotating case. The distance is fixed at $d = 80$ kpc. Middle left: The line of sight velocity distribution when rotation is included. A prograde rotating case is shown ($\eta = 0.1$) for two different longitudes. At large distances little difference is seen from the non-rotating case. Middle right: As the adjacent panel, but now the distance is fixed to $d = 30$ kpc. More pronounced rotation is seen at smaller distances. Bottom left: The line of sight distribution function for the prograde case at three different distances. The same line of sight as the top panels is chosen. Very small deviations from a non-rotating distribution are seen. The tangential and radial velocity distributions are shown by green and red lines respectively. Bottom right: The longitudinal velocity, v_l , distribution with the same parameters as the adjacent panel. Rotation is much more apparent in this case and the distribution is almost entirely skewed to negative v_l .

line of sight in question. The top right panel of Fig. 3 illustrates the dependence of $F(l, b, d, v_{\text{los}})$ on the power law index of the density profile, α . In a given gravitational potential, more extended tracer populations (smaller α) exhibit larger velocity dispersions than more centrally-concentrated ones.

The middle panels of Fig. 3 show the changes to the line of sight velocity distributions caused by the introduction of rotation. At large distances ($d \sim 80$ kpc) the rotating distribution is hardly distinguishable from the non-rotating case (as $v_{\text{los}} \approx v_r$). As expected, radially biased velocity distributions show the smallest deviation from the non-rotating case, but even a tangentially biased system may only show small differences. At smaller distances ($d \sim 30$ kpc) the profile depends on the particular line of sight as illustrated in the middle right panel.

The bottom panels show the line of sight velocity distribution and the longitudinal velocity distribution for prograde rotating systems ($\eta = 0.1$). We see that with just the line of sight velocity, the rotation of a system may be difficult to constrain. In particular, if the line of sight component of velocity is largely due to the radial component, then we can only poorly constrain rotation. However, applications where the line of sight velocity has significant contributions from the tangential velocity components, as for example in the case of M31, can give a more robust prediction for the rotation. The bottom right panel shows the distribution as a function of v_l . In this case, the distributions show much more pronounced differences from the non-rotating case. For this particular line of sight and with $\eta = 0.1$, the distribution is almost entirely skewed to negative v_l . This has important implications for the relevance of accurate proper motion measurements. The components of motion perpendicular to the line of sight can give conclusive evidence for rotation, whilst the deductions from the line of sight velocities rely heavily on the particular line of sight.

3 APPLICATIONS: THE MILKY WAY GALAXY

In this section, we apply our distribution functions to halo populations in the Milky Way Galaxy. Observed heliocentric velocities are converted to Galactocentric ones by assuming a circular speed of 220 km s^{-1} at the position of the sun ($R_0 = 8.5$ kpc) with a solar peculiar motion $(U, V, W) = (11.1, 12.24, 7.25) \text{ km s}^{-1}$ (recently updated by Schönrich et al. 2010). Here, U is directed toward the Galactic centre, V is positive in the direction of Galactic rotation and W is positive towards the North Galactic Pole.

We set the power law indices for the potential and density to $\gamma = 0.5$ and $\alpha = 3.5$ respectively. We allow the anisotropy β and rotation η parameters to be estimated by maximum likelihood analysis of the data. For example, when we have full distance information and the line of sight velocity, we construct the likelihood function from the LOSVD:

$$L(\eta, \beta) = \prod_{i=1}^N \log F(l_i, b_i, d_i, v_{\text{los}_i}, \eta, \beta), \quad (8)$$

where N is the number of objects in the population. Eqn (8) gives the two dimensional likelihood as a function of β and η . As we are mainly interested in constraining rotation, we sometimes fix β and find the likelihood as a function of η .

3.1 Milky Way BHB stars

Blue Horizontal Branch (BHB) stars are excellent tracers of halo dynamics as they are luminous and have an almost constant abso-

lute magnitude (within a certain colour range). We construct a sample of BHB stars from the Sloan Digital Sky Survey (SDSS) DR7 release. To select BHBs, we impose constraints on the (extinction corrected) $u - g$ and $g - r$ colours, the surface gravity (g_s) and the effective temperature (T_{eff}), namely:

$$\begin{aligned} 0.8 < u - g < 1.4 \\ -0.4 < g - r < 0 \\ 2 < \log(g_s) < 4 \\ 7250 < T_{\text{eff}}/\text{K} < 9700 \end{aligned} \quad (9)$$

These cuts are similar to those used by previous authors (e.g. Yanny et al. 2000, Sirko et al. 2004a) and are implemented to minimise contamination by blue stragglers and main sequence stars. We only consider stars with $|z| > 4$ kpc, as we wish to exclude disc stars. Xue et al. (2008) compiled a sample of 2558 BHB stars from SDSS DR6 using Balmer line profiles to select suitable candidates. Our larger sample (as we use the DR7 release) of 5525 stars includes $\approx 88\%$ of the Xue sample.

Heliocentric distances are evaluated photometrically by assuming BHBs have an absolute magnitude of $M_g = 0.7$ in the g band¹. The absolute magnitudes of BHB stars are slightly affected by temperature and metallicity (e.g. Sirko et al. 2004a) but we expect that this variation makes a negligible difference to our distance estimates. We compare our distance estimates to those of Xue et al. (2008), who take into account such variations, and find agreement to within 10%.

We remove contamination of stars belonging to the Sagittarius dwarf galaxy by masking out tracers lying in the region of the leading and trailing arms. Our final sample contains 3549 BHB stars (with $r > 10$ kpc) and so provides a statistically representative population to study the outer stellar halo. The heliocentric velocity errors are $\approx 5 \text{ km s}^{-1}$ on average, at larger radii the error increases due to the decreasing brightness of the source. The maximum error in the velocity is $\approx 20 \text{ km s}^{-1}$.

We use the metallicities derived from the Wilhelm et al. (1999) analysis (the ‘WBG’ method) as this method was adopted specifically for BHB stars. The method uses the CaII K lines as a metal abundance indicator and is applicable in the range $-3 < [\text{Fe}/\text{H}] < 0$. Only a small fraction ($N \sim 300$) of stars do not have assigned metallicities or are outside the applicable metallicity range.

Fig. 4 shows that the *overall* population (purple contour) has slight net retrograde rotation ($\eta = 1.1$) and has an almost isotropic distribution. By splitting the sample into metal-poor ($[\text{Fe}/\text{H}] < -2$, blue contours) and ‘metal-rich’ ($[\text{Fe}/\text{H}] > -2$, red contours) subsamples, we find retrograde and prograde signals for the two subsets respectively. The mean streaming motions for the metal-poor and metal-rich samples are $\langle v_\phi \rangle = -(35 \pm 10)(r/10 \text{ kpc})^{-1/4} \text{ km s}^{-1}$ and $\langle v_\phi \rangle = (21 \pm 11)(r/10 \text{ kpc})^{-1/4} \text{ km s}^{-1}$ respectively. We remove the radial dependence by averaging over the volume interval ($10 < r/\text{kpc} < 50$) to find $\langle v_\phi \rangle = -(25 \pm 7) \text{ km s}^{-1}$ and $\langle v_\phi \rangle = (15 \pm 8) \text{ km s}^{-1}$ for the metal-poor and metal-rich populations respectively. These results can be compared to Carollo et al. (2007) who find a rotating retrograde outer halo and a weakly prograde rotating inner halo. Our analysis only applies to the outer halo, but instead of a single population with net retrograde rotation, we find evidence for

¹ We check that changing our assumed absolute magnitude from $M_g = 0.7$ to $M_g = 0.55$ makes a negligible difference to our dynamical analysis.

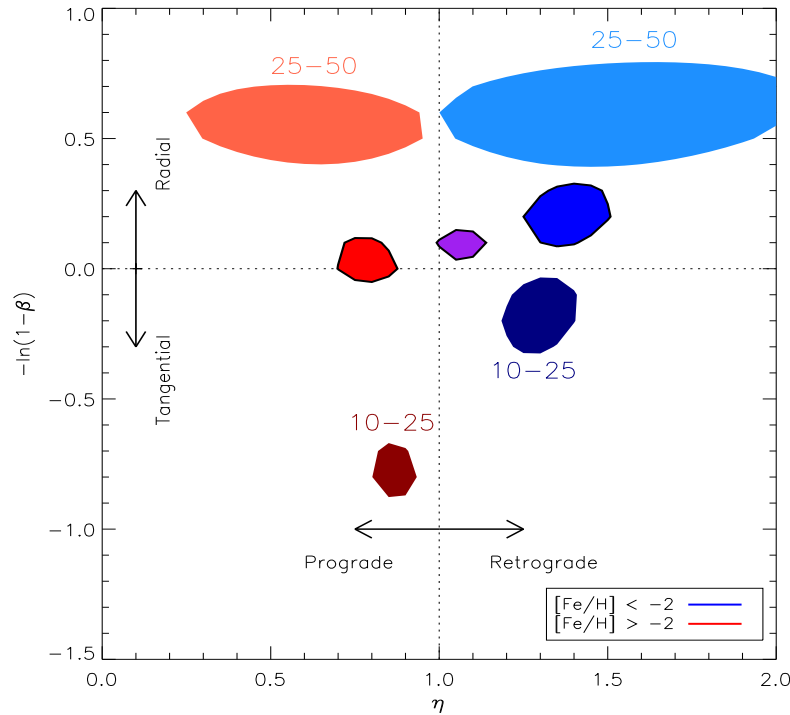


Figure 4. 1σ confidence regions for Milky Way halo BHB stars in the η, β plane from a maximum likelihood analysis. Arrows indicate prograde, retrograde, tangential and radial distributions respectively. The overall population ($N = 3549$ with $r > 10$ kpc) is shown by the purple filled contour. Metal poor ($[\text{Fe}/\text{H}] < -2$, $N = 1135$) and metal ‘rich’ ($[\text{Fe}/\text{H}] > -2$, $N = 2125$) subsamples are shown by blue and red contours respectively. The paler shades show the radial bin $25 < r/\text{kpc} < 50$ whilst the darker shades show the radial bin $10 < r/\text{kpc} < 25$.

two separate populations split by metallicity (at $[\text{Fe}/\text{H}] \sim -2$). In agreement with Carollo et al. (2007) (who focus on halo stars within the solar circle) we find evidence for a net retrograde rotating metal-poor halo component, but we find that the outer halo also contains a more metal-rich slightly prograde-rotating component.

We can make a rough estimate of the luminosity associated with these metal-rich and metal-poor remnants assuming 40% of the metal-poor sample ($\eta \sim 1.4$, $N_{\text{poor}} = 1135$) and 20% of the metal-rich sample ($\eta \sim 0.8$, $N_{\text{rich}} = 2125$) are rotating. The fraction of rotating stars can be scaled to the overall population by calculating the total number of BHBs in a spherical volume. This requires a normalisation factor for our density profile ($\rho \propto r^{-3.5}$). We adopt the normalisation applicable to RR Lyrae stars found by Watkins et al. (2009) and assume the ratio of BHBs to RR Lyrae is approximately 2:1. Finally, using photometry for globular clusters given in An et al. (2008), we find the relation $N_{\text{BHB}}/L \sim 10^{-3} L_{\odot}^{-1}$ (where N_{BHB} is found by applying a cut in colour-colour space - see eqn 9). We find for both the metal-poor and metal-rich rotating populations a luminosity $L \sim 10^8 L_{\odot}$. For a mass to light ratio of $M/L \sim 10$ (appropriate for luminous satellites - see Fig. 9 in Mateo 1998) this gives a total mass estimate of $M \sim 10^9 M_{\odot}$. This rough calculation suggests that these rotating signals could be remnants of two separate accretion events caused by massive satellites with different metallicities and orbital orientations.

The different shaded contours in Fig. 4 show different radial bins. The paler shades are for the range $25 < r/\text{kpc} < 50$ whilst the darker shades are for the range $10 < r/\text{kpc} < 25$. Splitting the sample into radial bins shows the rotation signal is present at all radii (albeit with less confidence at greater distances due to smaller

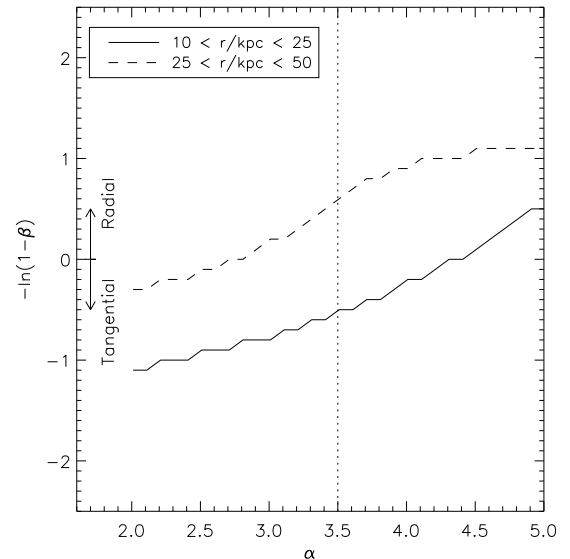


Figure 5. The variation in the anisotropy parameter β with the density profile index α for Milky Way halo BHB stars. The solid line and dashed lines are for the radial bins, $10 < r/\text{kpc} < 25$ ($N = 2312$) and $25 < r/\text{kpc} < 50$ ($N = 1127$) respectively. More steeply declining density profiles (larger α) give more radially anisotropic β values. Arrows represent tangential and radial distributions respectively.

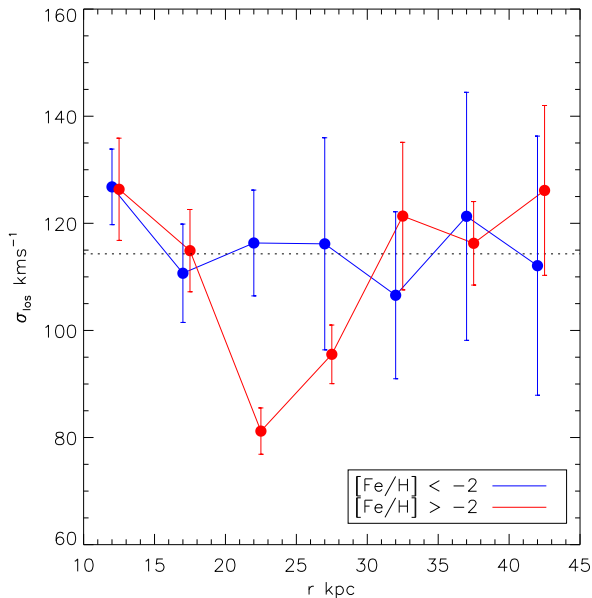


Figure 6. Line of sight velocity dispersion as a function of Galactocentric radii for Milky Way halo BHB stars. The metal poor ($[\text{Fe}/\text{H}] < -2$) and metal rich ($[\text{Fe}/\text{H}] > -2$) components are given by the blue and red lines respectively. An obvious cold feature is apparent in the metal rich population at $r \sim 25$ kpc. The dotted line is the average σ_{los} for the whole population.

numbers) but also shows that the velocity distribution becomes more radially biased with increasing Galactocentric radii. This result is in agreement with the findings of cosmological simulations (e.g. Diemand et al. 2007; Sales et al. 2007). Stars populating the outer halo are likely remnants of merger events and therefore can be on eccentric orbits. However, the anisotropy parameter β is dependent on the adopted density profile (whereas the rotation parameter η is independent). More centrally located populations (larger α) exhibit narrower velocity dispersions (see Section 2). To compensate for the narrower velocity dispersion the unknown tangential distribution shrinks as we only have a measurement for the line of sight velocity. Hence, the distribution becomes more radially anisotropic (β increases) when we adopt steeper density power laws. This is shown in Fig. 5 for two radial bins. To break this degeneracy we require a full analysis of the density profile of the BHB sample. As our main result regarding rotation is unaffected we defer this task to a future paper.

Evidence for substructure in the metal-rich sample is shown in Fig. 6. Here, we show the line of sight velocity dispersion, σ_{los} , as a function of Galactocentric radii. We formulate error bars by assuming Gaussian distributed errors and apply a maximum likelihood routine to find the 1σ deviations. There is an obvious ‘cold’ structure in the metal-rich sample for $20 < r/\text{kpc} < 30$. This could be evidence for a shell type structure caused by a relatively recent accretion event. The lack of such a feature in the metal-poor sample suggests that the net retrograde signal is not a consequence of a single accretion event. The dichotomous nature of the outer halo may reflect two populations with very different origins. This is discussed further in Section 4.

We note that a larger sample of BHB stars extending to larger Galactocentric distances, will be invaluable in studying the outer reaches of the stellar halo. To date very few tracers are available,

but future spectroscopic surveys are likely to increase the sample of distant BHBs with measured velocities. For example the proposed LSST mission, will provide a vast number of spectroscopic targets out to a magnitude limit of $r \sim 27$.

3.2 Milky Way globular clusters

The kinematics of the Milky Way globular clusters have been studied by a number of authors (e.g. Frenk & White 1980; Zinn 1985). We apply the methods adopted in the previous section to model the halo globular clusters. Using the data taken from Harris (1996), we restrict attention to those at galactocentric distances $r > 10$ kpc.

With line of sight velocities alone, our sample of 41 globular clusters poorly constrains β and η . We improve this analysis using the proper motion measurements from Dinescu et al. (1999) and Casetti-Dinescu et al. (2007), which include 15 of our halo clusters (see Table 2). We use a similar procedure to Wilkinson & Evans (1999) and convolve our probabilities with an error function. Eqn (7) becomes

$$F(l, b, d, v_{\text{los}}) = \int \int E_1(v_l) E_1(v_b) \times F(l, b, d, v_l, v_b, v_{\text{los}}) dv_l dv_b, \quad (10)$$

where $E_1(v)$ is the error function. We assume the Lorentzian given by

$$E_1(v) = \frac{1}{\sqrt{2\pi}\sigma_1} \frac{2\sigma_1^2}{2\sigma_1^2 + (v - v_{\text{obs}})^2}, \quad (11)$$

where σ_1 is related to the published error estimate by $\sigma_1 = 0.477\sigma_{\text{meas}}$. The properties of such functions are discussed further in Appendix A of Wilkinson & Evans (1999). We show in the left hand panel of Fig. 7 that the halo clusters have a mildly radial distribution ($\beta = 0.5_{-0.3}^{+0.1}$) and net prograde rotation ($\eta = 0.3_{-0.3}^{+0.35}$). We find a mean streaming motion of $\langle v_\phi \rangle = (58 \pm 27)(r/10\text{kpc})^{-1/4} \text{ km s}^{-1}$ which evaluates to $\langle v_\phi \rangle \sim (60 - 50) \text{ km s}^{-1}$ in the range $r = (10 - 20) \text{ kpc}$. This agrees with previous authors (e.g. Frenk & White 1980; Zinn 1985) who have found that the halo globular clusters are primarily pressure supported, but show weak rotation with $v_{\text{rot}} \sim 50 - 60 \text{ km s}^{-1}$.

The right panel of Fig. 7 shows the v_ϕ velocity components of the globular clusters overplotted on a mildly radial model for $\langle v_\phi(r) \rangle$. The majority of the globular clusters have positive v_ϕ and hence the net streaming motion is prograde. However, 5 of the halo globular clusters have negative v_ϕ . As our sample only consists of 15 objects, we cannot conclude that this net prograde rotation is ubiquitous for the whole population. There is no obvious correlation between rotational velocity and metallicity, suggesting independent accretion events rather than dissipative collapse as the formation mechanism.

The majority of the halo globular clusters in our sample have metallicities between $-2 < [\text{Fe}/\text{H}] < -1$ and Galactocentric radii in the range $10 < r/\text{kpc} < 20$ (with the notable exception of Pal 3). It is interesting that these properties are in common with the relatively metal-rich halo BHB stars, which also exhibit net prograde rotation (albeit a weaker signal). We suggest that some of the globular clusters with positive v_ϕ may share a common accretion history with these relatively metal-rich field halo stars.

Name	r (kpc)	[Fe/H]	v_h (kms $^{-1}$)	$\mu_\alpha \cos(\delta)$ (mas yr $^{-1}$)	μ_δ (mas yr $^{-1}$)	v_ϕ (kms $^{-1}$)	Ref
NGC 288	11.8	-1.24	-46.6	4.40 ± 0.23	-5.62 ± 0.23	-27 ± 18	1,2
NGC 1851	17.2	-1.26	320.9	1.28 ± 0.68	2.39 ± 0.65	134 ± 29	1,2
NGC 1904	18.9	-1.54	207.5	2.12 ± 0.64	-0.02 ± 0.64	83 ± 29	1,2
NGC 2298	16.0	-1.85	148.9	4.05 ± 1.00	-1.72 ± 0.98	-27 ± 30	1,2
NGC 2808	11.2	-1.37	93.6	0.58 ± 0.45	2.06 ± 0.46	82 ± 16	1,3
NGC 4147	21.1	-1.83	183.2	-1.85 ± 0.82	-1.30 ± 0.82	67 ± 65	1,2
NGC 4590	10.3	-2.06	-95.2	-3.76 ± 0.66	1.79 ± 0.62	294 ± 30	1,2
NGC 5024	19.0	-2.07	-79.1	0.50 ± 1.00	-0.10 ± 1.00	240 ± 85	1,2
NGC 5272	12.1	-1.57	-148.6	-1.10 ± 0.51	-2.30 ± 0.54	105 ± 24	1,2
NGC 5466	17.0	-2.22	107.7	-4.65 ± 0.82	0.80 ± 0.82	-63 ± 64	1,2
NGC 6934	12.4	-1.54	-411.4	1.20 ± 1.00	-5.10 ± 1.00	-67 ± 60	1,2
NGC 7078	10.5	-2.22	-107.5	-0.95 ± 0.51	-5.63 ± 0.50	129 ± 25	1,2
NGC 7089	10.4	-1.62	-5.3	5.90 ± 0.86	-4.95 ± 0.86	-84 ± 41	1,2
Pal 3	92.9	-1.66	83.4	0.33 ± 0.23	0.30 ± 0.31	146 ± 95	1,2
Pal 5	17.8	-1.38	-55.0	-1.78 ± 0.17	-2.32 ± 0.23	42 ± 34	1,2

Table 2. The Milky Way halo globular cluster sample with available proper motions. We give the Galactocentric radii r (note we correct the Harris (1996) values to a solar position of $R_\odot = 8.5$ kpc), the metallicity [Fe/H], the heliocentric velocity, v_h , the heliocentric rest frame proper motions in right ascension and declination and the rotational velocity, v_ϕ . References: (1) Harris (1996), (2) Dinescu et al. (1999), (3) Casetti-Dinescu et al. (2007).

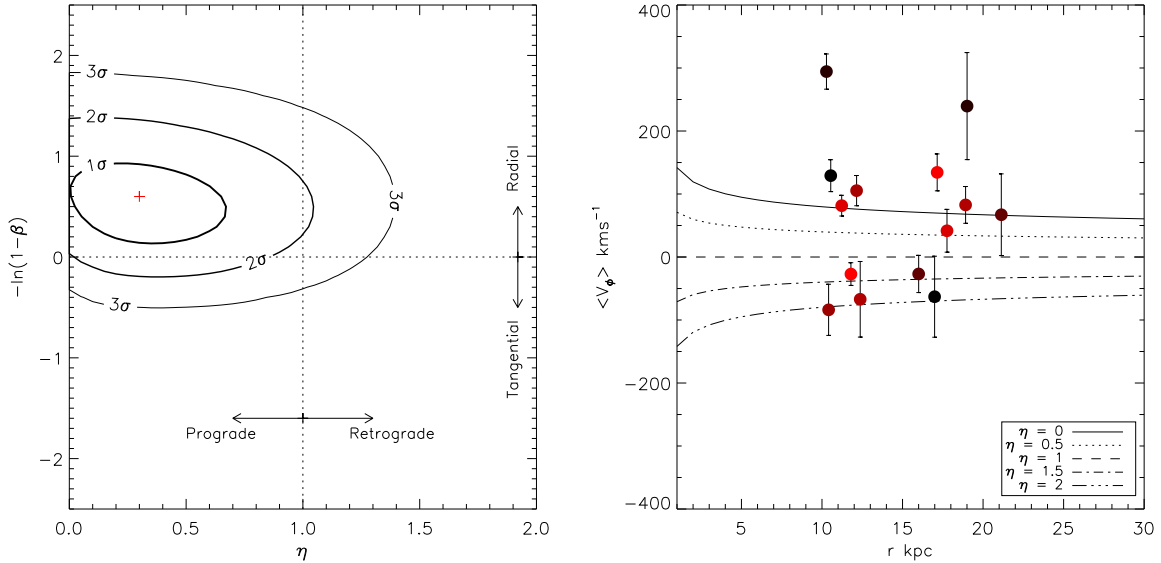


Figure 7. Left: The confidence contours for Milky Way halo globular clusters in the η, β plane evaluated from a 2D Maximum likelihood analysis. Arrows illustrate prograde, retrograde, radial and tangential distributions respectively. We use $-\ln(1 - \beta)$ on the y-axis to make the ranges occupied by radial and tangential models symmetric. The Milky Way globular clusters with available proper motions ($N = 15$) show evidence for prograde rotation ($\eta \sim 0.3$) and a mildly radial velocity distribution ($\beta \sim 0.5$). Right: The streaming motion as a function of Galactocentric radius for a mildly radial distribution $\beta = 0.5$ (see Fig. 2). Different linestyles represent different rotation parameters (η). Overplotted are the v_ϕ velocity components of the Milky Way globular clusters with available proper motions. The points are colour coded according to metallicity, black being the most metal-poor ([Fe/H] ~ -2.2) and red being the most metal-rich ([Fe/H] ~ -1.2). There is no obvious correlation with metallicity but the two clusters with particularly large positive v_ϕ ($\sim 200 - 300$ kms $^{-1}$), NGC 4590 and NGC 5024, are also metal poor ([Fe/H] < -2). Note that ~ 5 of the globular clusters have negative v_ϕ , but the majority have positive v_ϕ . As there are only 15 objects in the sample the net prograde motion may not be representative of the whole population. Pal 3 is not shown as its distance of $r \sim 90$ kpc is beyond the range of the plot, but note that it too has a positive v_ϕ (albeit with large formal uncertainties, 146 ± 95 kms $^{-1}$)

3.3 Milky Way Satellites

Our final application focusing on our own Milky Way Galaxy looks at the satellite galaxies. Fig. 8 shows the result of the maximum likelihood analysis keeping the velocity anisotropy fixed at $\beta = 0$. We have split the satellites into classical ($L \sim 10^6 L_\odot$) and ultra-faint ($L \sim 10^2 - 10^4 L_\odot$) samples (see Tables 4 and 3). There is some controversy as to whether these groups are separate populations or just the bright and faint components of a single population. We can see from Fig. 8 that the rotation is poorly con-

strained. The 1σ confidence limit (horizontal dotted line) encompasses non-rotating, retrograde and prograde solutions. We illustrate the isotropic case ($\beta = 0$) in Fig. 8 but the same form is seen for radial or tangential distributions.

To make further progress, we incorporate the available proper motion data of the Milky Way satellites into the analysis. This restricts the analysis to the classical satellites, as no proper motion measurements are available for the ultra-faints. Fig. 9 (left panel) shows the resulting likelihood distribution with respect to the rotation parameter, η and the anisotropy parameter, β .

Name	l ($^\circ$)	b ($^\circ$)	d (kpc)	v_h (kms $^{-1}$)	μ_α (mas cent $^{-1}$)	μ_δ (mas cent $^{-1}$)	v_ϕ (kms $^{-1}$)	Ref
Carina	260.0	-22.2	101.0	224.0	22 ± 9	15 ± 9	68 ± 43	1,2
Fornax	237.1	-65.7	138.0	53.0	48 ± 5	-36 ± 4	-76 ± 27	1,3
Draco	86.4	34.7	82.0	-293.0	19 ± 13	-3 ± 12	17 ± 47	1,4
Leo I	226.0	49.1	250.0	286.0	-	-	-	1
Leo II	220.2	67.2	205.0	76.0	-	-	-	1
LMC	280.5	-32.9	50.0	278.0	196 ± 4	44 ± 4	82 ± 8	5,6
Sagittarius	5.6	-14.1	24.0	140.0	-283 ± 20	-133 ± 20	49 ± 22	1,7
Sculptor	287.5	-83.2	79.0	108.0	9 ± 13	2 ± 13	126 ± 49	1,8
Sextans	243.5	42.3	86.0	227.0	-26 ± 41	10 ± 44	193 ± 153	1,9
SMC	302.8	-44.3	60.0	158.0	75 ± 6	-125 ± 6	44 ± 16	5,6
Ursa Min	105.0	44.8	66.0	-248.0	-50 ± 17	22 ± 16	-87 ± 48	1,10

Table 4. The properties of the classical Milky Way satellites. Here, we give the Galactic coordinates (l, b) , the heliocentric distance d , the heliocentric velocity v_h , and the heliocentric rest frame proper motions in right ascension and declination and the rotational velocity, v_ϕ . References: (1) Mateo 1998, (2) Piatek et al. 2003, (3) Piatek et al. 2007, (4) Piatek et al. 2008a, (5) Karachentsev et al. 2004, (6) Piatek et al. 2008b, (7) Dinescu et al. 2005, (8) Piatek et al. 2006, (9) Walker et al. 2008, (10) Piatek et al. 2005

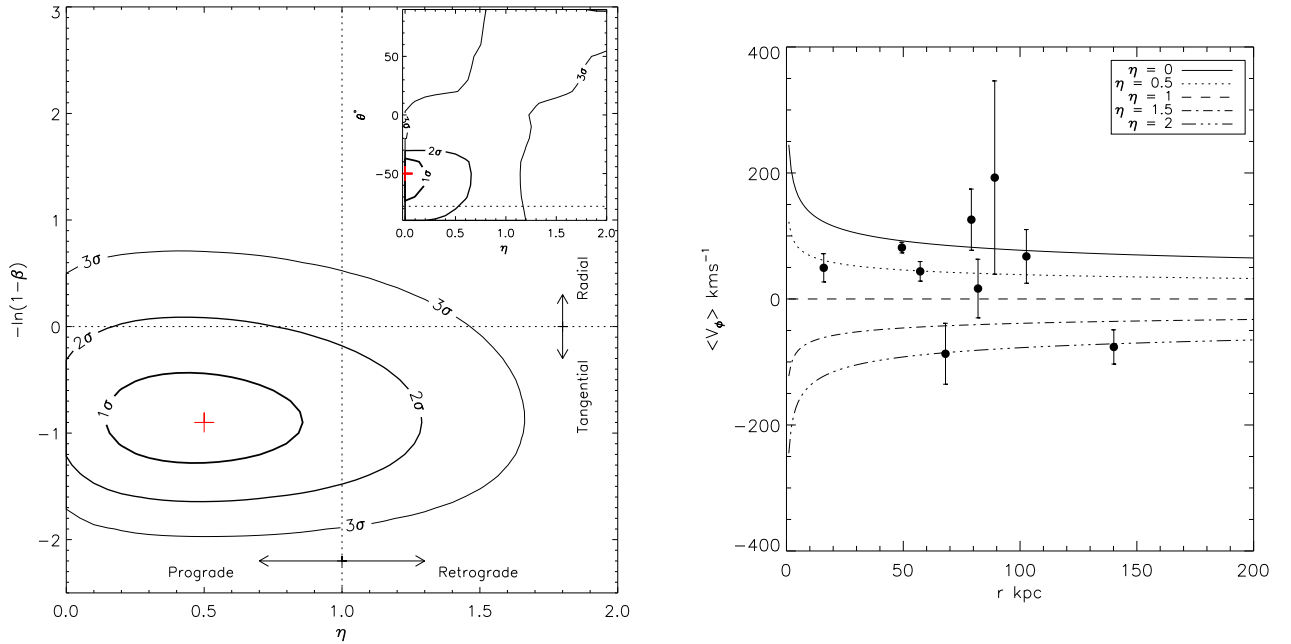


Figure 9. Left: The 2D η, β confidence contour plane for the Milky Way satellite galaxies from the maximum likelihood analysis. Arrows illustrate the regions of prograde, retrograde, radial and tangential distributions respectively. The Milky Way satellites with available proper motions show evidence for prograde rotation ($\eta \sim 0.5$) and a tangential velocity distribution ($\beta \sim -1.5$). The inset of the figure shows the confidence contours when the normal vector of the angular momentum is tilted with respect to the Milky Way disc (by an angle θ). More pronounced prograde rotation is seen when $\theta \approx -50^\circ$. The dotted line shows the approximate tilt angle found by Metz et al. (2007) using spatial coordinates of the satellites assuming they form a ‘disc of satellites’. Right: The streaming motion as a function of Galactocentric radius for a tangential distribution $\beta = -1.5$ (see Fig. 2). Different line styles represent different rotation parameters (η). Overplotted are the v_ϕ velocity components of the Milky Way satellites with available proper motions. Most exhibit positive v_ϕ values but Fornax and Ursa Minor have negative v_ϕ .

With these extra constraints on the tangential velocity components, the maximum likelihood method gives evidence for prograde rotation ($\eta = 0.5^{+0.4}_{-0.2}$, $\beta = -1.5^{+0.7}_{-1.0}$). Evaluating eqn (6) gives $\langle v_\phi \rangle = (69 \pm 42)(r/10 \text{ kpc})^{-1/4} \text{ kms}^{-1}$. Averaging over the volume interval ($10 < r/\text{kpc} < 150$) gives $\langle v_\phi \rangle = (38 \pm 23) \text{ kms}^{-1}$. The right hand panel of Fig. 9 shows v_ϕ for the satellites with proper motion data overplotted on a tangential model for $\langle v_\phi(r) \rangle$ (see Fig. 2). Most of the satellites have prograde rotation components, although the Fornax and Ursa Minor satellites show retrograde rotation.

Watkins et al. (2010) recently reported $\beta = 0.44$ for the Milky Way satellites based on results of simulations by Diemand et al. 2007. However, based on the proper motion data, the same authors find $\beta \approx -4.5$, favouring tangential orbits. Our result also favours tangential orbits (in agreement with Wilkinson & Evans (1999) who find $\beta \approx -1$).

The orbits of the satellites for which we have all velocity components are preferentially polar (v_θ is the largest velocity component). This has been noted in earlier work (e.g Zaritsky & Gonzalez 1999) and has led to the suggestion that the Milky Way satellites

Name	l ($^{\circ}$)	b ($^{\circ}$)	d (kpc)	v_h (kms $^{-1}$)	Ref
Boo I	358.1	69.6	62.0	99.0	1
Boo II	353.7	68.9	46.0	-117.0	2
Can Ven I	74.3	79.8	224.0	30.9	3
Can Ven II	113.6	82.7	151.0	-128.0	3
Coma	241.9	83.6	44.0	98.1	3
Hercules	28.7	36.9	138.0	45.0	3
Leo IV	265.4	56.5	158.0	132.3	3
Leo V	261.9	58.5	180.0	173.3	4
Segue I	220.5	50.4	23.0	206.0	5
Segue II	149.4	-38.1	35.0	-39.2	6
Ursa Maj II	152.5	37.4	32.0	-116.5	3
Willman I	158.6	56.8	38.0	-12.3	1

Table 3. The properties of the ultra-faint Milky Way satellites. We give the Galactic coordinates (l , b), the heliocentric distance d , and the heliocentric velocity v_h . References: (1) Martin et al. 2007, (2) Koch et al. 2009, (3) Simon & Geha 2007, (4) Belokurov et al. 2008, (5) Geha et al. 2009, (6) Belokurov et al. 2009

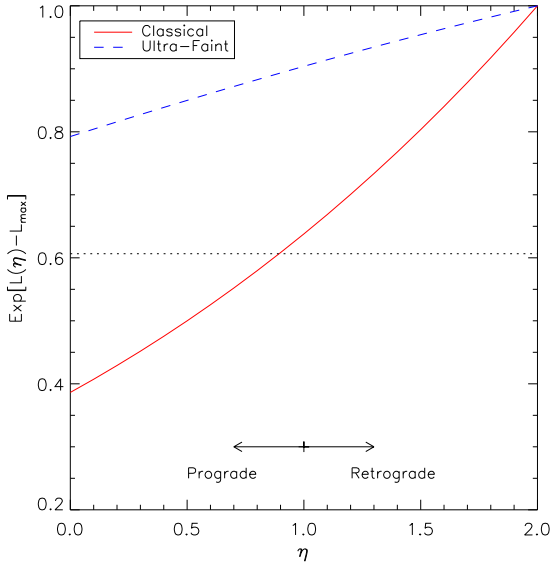


Figure 8. Maximum likelihood analysis of the rotation parameter, η , for Milky Way satellites. The velocity anisotropy is kept fixed at $\beta = 0$. The y-axis, $\text{Exp}[L(\eta) - L_{\text{max}}]$, is the reduction of the likelihood for a particular η value with respect to the maximum likelihood. The red (solid) and blue (dashed) lines represent the classical and ultra-faint satellites respectively. Rotation is poorly constrained in both cases.

may occupy a highly inclined disc of satellites (Palma et al. 2002; Kroupa et al. 2005; Metz et al. 2007). We have chosen the L_z angular momentum component of the ensemble of satellites to be aligned with that of the disc of the Milky Way. As an inset in the left hand panel of Fig. 9, we show how the apparent rotation changes if we introduce a tilted angular momentum vector for the ensemble of satellite galaxies ($-90^{\circ} < \theta < 90^{\circ}$). Note that $\theta = 0$ corresponds to alignment with the L_z angular momentum vector of the Milky Way disc. We find more pronounced (prograde) rotation when $\theta = -50^{\circ} {}^{+15}_{-20}$. This result is not surprising considering we find preferentially polar orbits, but does not necessarily mean the satellites occupy a rotationally supported disc. We also show the approximate tilt angle found by Metz et al. (2007) of $\theta \approx -78^{\circ}$

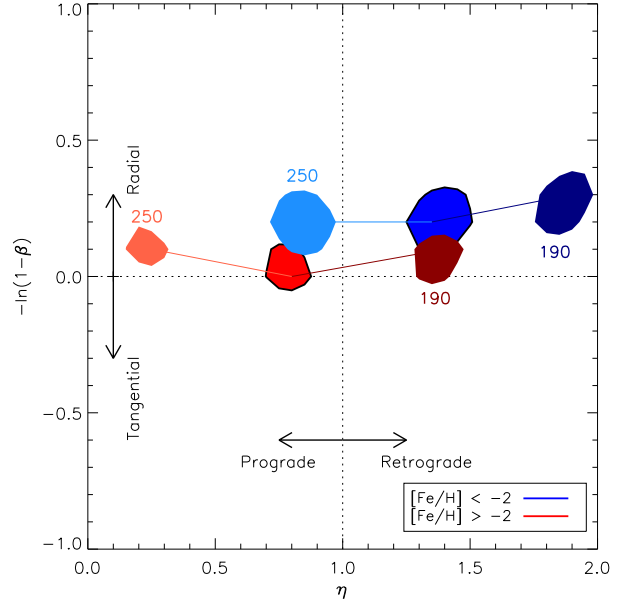


Figure 10. As Fig. 4 but we show the effects of varying the local standard of rest velocity (Θ_0). Metal poor ($[\text{Fe}/\text{H}] < -2$, $N = 1135$) and metal ‘rich’ ($[\text{Fe}/\text{H}] > -2$, $N = 2125$) subsamples are shown by blue and red contours respectively. The paler shades show an increase in the circular speed to $\Theta_0 = 250 \text{ kms}^{-1}$ whilst the darker shades show a decrease in the circular speed to $\Theta_0 = 190 \text{ kms}^{-1}$

(dotted line)². The authors find the spatial distribution of the satellites is best described by a highly inclined disc. Whilst our results favour a slightly less inclined plane, it is interesting that the deductions from both a kinematic and spatial analysis broadly agree. However, without more accurate proper motion measurements the disc of satellites hypothesis cannot be rigorously tested.

4 THE LOCAL STANDARD OF REST

Our interpretation of any rotation signal in the Milky Way stellar halo depends on our assumed local standard of rest rotational velocity (Θ_0). The IAU (International Astronomical Union) recommend a value of $\Theta_0 = 220 \text{ kms}^{-1}$. In practice, estimates of the rotation speed in the literature vary between 184 kms^{-1} (Olling & Merrifield 1998) and 272 kms^{-1} (Méndez et al. 1999). Many of these estimates are confined to regions within the solar neighbourhood and rely on assuming a value for the Galactocentric distance (R_0).

An abundance of evidence (net rotation, extent, metallicity, velocity, anisotropy, dispersion profile) suggests the relatively metal-rich BHB population of the Milky Way halo is associated with the accretion of a massive satellite. The low metallicity and flat velocity dispersion profile of the metal-poor population argue against an association with a single accretion event. We infer that this metal-poor population reflects the ‘primordial’ metal-poor halo. The net retrograde rotation may simply be the result of an *underestimate* of the local standard of rest rotational velocity. In Fig. 10 we show the effect of varying Θ_0 on our results for the Milky

² There is a typo in the abstract of Metz et al. (2007) where an inclination angle of 88° is given instead of the (correct) value of 78°

Way halo BHB population (see Fig. 4). Increasing our adopted Θ_0 value removes any retrograde signal in the metal-poor population and enhances the net prograde signal for the metal-rich population. We can provide functional forms for the rotation signal of the two components by fitting a simple linear relation to the adopted local standard of rest value:

$$\begin{aligned} \langle v_\phi \rangle_{\text{poor}} &= \left(275 \left[\frac{\Theta_0}{220} \right] - 300 \right) \text{ kms}^{-1} \\ \langle v_\phi \rangle_{\text{rich}} &= \left(330 \left[\frac{\Theta_0}{220} \right] - 315 \right) \text{ kms}^{-1} \quad (12) \\ 190 &< \Theta_0 / \text{kms}^{-1} < 250 \end{aligned}$$

Here we have removed the dependence on Galactocentric radii of $\langle v_\phi \rangle$ (see eqn 6) by integrating over the appropriate volume interval ($10 < r/\text{kpc} < 50$). If we assume the metal-poor halo component has no net rotation, then we can infer an independent estimate for the local standard of rest rotational velocity of $\Theta_0 \approx 240 \text{ kms}^{-1}$.

An upward revision of the commonly adopted circular speed of 220 kms^{-1} agrees with recent work by Reid et al. (2009) and Bovy et al. (2009) based on the kinematics of masers found in massive star-forming regions of the Milky Way. Reid et al. (2009) fit for R_0 and Θ_0 simultaneously using kinematic and spatial information on sources well beyond the local solar neighbourhood and established a circular rotation speed, $\Theta_0 \approx 250 \text{ kms}^{-1}$. Bovy et al. (2009) re-analysed the maser tracers using less restrictive models and found a rotation speed of $\Theta_0 \approx 240 - 250 \text{ kms}^{-1}$. They confirm that there is no conflict between recent determinations of the circular rotation speed based on different methods (e.g. orbital fitting of the GD-1 stellar stream, see Koposov et al. 2010) and quote a combined estimate of $\Theta_0 \approx 240 \text{ kms}^{-1}$.

Note that Carollo et al. (2007) argued that the net retrograde signal in the outer halo ($r > 10 \text{ kpc}$) is due to dynamical friction effects. Quinn & Goodman (1986) show, based on the effects of dynamical friction, that fragments on retrograde orbits surrender their orbital energy to a much smaller extent than those on prograde orbits. The disintegration of many of these fragments by tidal forces may result in the formation of a halo stellar population with a net retrograde asymmetry (e.g. Norris & Ryan 1989). Hence, in this picture the metal-poor component is the accumulation of several (smaller) accretion events. However, it is questionable whether this is a plausible explanation seeing as dynamical friction mainly affects massive satellites close to the plane of the disc. This is difficult to reconcile with the aggregation of less massive satellites which leave debris over a wide range of distances ($10 < r/\text{kpc} < 50$) studied in this work.

We conclude that the lack of a plausible physical explanation for a net retrograde rotating metal-poor halo population suggests that the commonly adopted local standard of rest circular velocity needs to be revised upwards. Assuming the primordial metal-poor halo has no net rotation provides an independent estimate for this fundamental Galactic parameter.

5 APPLICATIONS: THE ANDROMEDA GALAXY

We now apply our analysis to the Andromeda (M31) galaxy. In this case, we transform to a coordinate system centred on M31. We define the projected distances (in angular units) along the major and

Name	Type	l ($^\circ$)	b ($^\circ$)	d (kpc)	v_h kms^{-1}	Ref
M31	Spiral	121.2	-21.6	785_{-25}^{+25}	-301	1
And I*	dSph	121.7	-24.8	745_{-24}^{+24}	-380	1
And II*	dSph	128.9	-29.2	652_{-18}^{+18}	-188	1
And III*	dSph	119.4	-26.3	749_{-24}^{+24}	-355	1
And V	dSph	126.2	-15.1	774_{-28}^{+28}	-403	1
And VI*	dSph	106.0	-36.3	783_{-25}^{+25}	-354	1
And VII	dSph	109.5	-9.9	763_{-25}^{+25}	-307	1
And IX*	dSph	123.2	-19.7	765_{-150}^{+5}	-207.7	2
And X*	dSph	125.8	-18.0	702_{-36}^{+36}	-163.8	3,4
And XI*	dSph	121.7	-29.0	760_{-150}^{+10}	-419.6	2
And XII*	dSph	122.0	-29.5	830_{-30}^{+170}	-558.4	2
And XIII*	dSph	123.0	-29.9	910_{-160}^{+30}	-195.0	2
And XIV*	dSph	123.0	-33.2	740_{-110}^{+110}	-481.1	5
And XV*	dSph	127.9	-24.5	770_{-70}^{+70}	-339	6
And XVI	dSph	124.9	-30.5	525_{-50}^{+50}	-385	6
Pisces	dIrr/dSph	126.8	-40.9	769_{-23}^{+23}	-286	1
Pegasus	dIrr/dSph	94.8	-43.6	919_{-30}^{+30}	-182	1
NGC 147	dE	119.8	-14.3	675_{-27}^{+27}	-193	1
IC 1613	dE	129.8	-60.6	700_{-35}^{+35}	-232	1
NGC 185	dE	120.79	-14.5	616_{-26}^{+26}	-202	1
NGC 205	dE	120.7	-21.1	824_{-27}^{+27}	-244	1
IC 10	dIrr	119.0	-3.3	825_{-50}^{+50}	-344	1
M32	cE	121.2	-22.0	785_{-25}^{+25}	-205	1

Table 5. Properties of the Andromeda Satellites: Here, we give the satellite name and type (dSph = dwarf spheroidal, dIrr = dwarf irregular, dE = dwarf elliptical and cE = classical elliptical), Galactic coordinates (l, b), heliocentric distance d and heliocentric velocity v_h . Satellites belonging to the rotating group are starred. References: (1) McConnachie & Irwin 2006, (2) Collins et al. 2009, (3) Zucker & et al 2007, (4) Kalirai et al. 2009, (5) Majewski et al. 2007, (6) Letarte et al. 2009

minor axis, X and Y via:

$$\begin{aligned} x_0 &= \sin(\alpha - \alpha_0) \cos(\delta), \\ y_0 &= \sin(\delta) \cos(\delta_0) - \cos(\alpha - \alpha_0) \cos(\delta) \sin(\delta_0), \\ X &= x_0 \sin(\theta_a) + y_0 \cos(\theta_a), \\ Y &= -x_0 \cos(\theta_a) + y_0 \sin(\theta_a), \end{aligned} \quad (13)$$

where x_0, y_0 are Cartesian coordinates for α, δ with respect to the centre of M31 ($\alpha_0 = 00^{\text{h}}42^{\text{m}}44.3^{\text{s}}$ $\delta_0 = +41^\circ 16' 09''$; Cotton et al. 1999) and $\theta_a = 37.7^\circ$ (de Vaucouleurs 1958) is the position angle. We adopt the transformation outlined in Appendix A of Evans & de Zeeuw (1994) to relate the projected coordinates to the galaxy coordinates (assuming an inclination angle, $i = 77.5^\circ$).

5.1 M31 Satellites

The main drawback in the M31 analysis is that the distances to the satellites are not as well constrained as for the Milky Way satellites. To take this into account, we integrate the distribution function along the line of sight between the distance errors. The left hand panel of Fig. 11 shows the results of the maximum likelihood analysis applied to all of the M31 satellites (see Table 5). Unlike the situation for the Milky Way satellites, our line of sight

to M31 is not constrained to a predominantly radial velocity component. Fig. 11 shows evidence of prograde rotation from the line of sight velocity alone. We further investigate this rotating component by splitting the M31 sample into two groups based on the satellite type. These are shown by the red (dSph) and blue points (non-dSph) in Fig. 11 where we find a rotating group (dSph, red) and a non-rotating group (non-dSph, blue). The rotating subset has a rotation parameter, $\eta = 0.4^{+0.3}_{-0.3}$ and anisotropy parameter, $\beta = 0.1^{+0.5}_{-0.5}$, which corresponds to a streaming motion, $\langle v_\phi \rangle = (62 \pm 34)(r/10 \text{ kpc})^{-1/4} \text{ kms}^{-1}$. Averaging over a suitable volume interval ($10 < r/\text{kpc} < 200$) gives $\langle v_\phi \rangle = (32 \pm 17) \text{ kms}^{-1}$.

The observed line of sight velocities of the M31 satellites can be decomposed into radial and tangential components by making use of the spatial information relative to M31. These are lower limits as we only have the line of sight velocity component (see Metz et al. 2007). There are also large uncertainties on the distances of the satellites which permeate into the spatial coordinates with respect to M31. However, we still find it instructive to look at these approximate velocity components. The right panel of Fig. 11 shows the lower limit tangential and radial velocity components for the M31 satellites. The members of the dSph rotating group are shown by red stars and the non-rotating satellites are shown by the blue circles. The majority of the rotating subgroup have a larger tangential velocity than radial velocity component.

The rotating subgroup consists entirely of dwarf spheroidal galaxies. Satellites with similar accretion histories can share common properties such as their ‘type’ (i.e dSph) and orbital orientation. The apparent rotation of the dSph satellites of M31 suggests that these dwarfs may share a common origin.

5.2 M31 globular clusters

Over recent years, studies by several authors (e.g. Perrett et al. 2002, Galleti et al. 2007, Kim et al. 2007, Caldwell et al. 2009) have produced a rich sample of M31 globular clusters with available kinematic data. Our data derives from the Revised Bologna Catalogue (Galleti et al. 2004). Distance measurements are unavailable for the globular clusters, so we integrate our distribution function along the line of sight.

We consider the 93 globular clusters for which the projected distance along the semi-minor axis is greater than 5 kpc ($|Y| > 5 \text{ kpc}$). This criterion was introduced by Lee et al. (2008). For 54 of these clusters, metallicities are available and so we further divide the sample into 24 metal-rich ($[\text{Fe}/\text{H}] > -1$) and 30 metal-poor ($[\text{Fe}/\text{H}] < -1$) components. Fig. 12 shows the outer M31 globular clusters are rotating prograde with respect to the M31 disc. The metal-rich subset (solid red contours) has $\eta = 0^{+0.2}_{-0.2}$ and $\beta = 0.3^{+0.4}_{-0.6}$ giving a streaming motion, $\langle v_\phi \rangle = (94 \pm 35)(r/10 \text{ kpc})^{-1/4} \text{ kms}^{-1}$. The metal-poor subset (dashed blue contours) has a less pronounced rotation with $\eta = 0.1 \pm 0.5$, and a more pronounced radial anisotropy, $\beta = 0.7^{+0.1}_{-0.2}$. This indicates that it has a smaller streaming velocity: $\langle v_\phi \rangle = (53 \pm 34)(r/10 \text{ kpc})^{-1/4} \text{ kms}^{-1}$. However, the broad overlap of the 1σ error envelopes of these samples mean that it is premature to conclude that we are indeed seeing a significant difference between the metal-rich and metal-poor populations. Lee et al. (2008) also find strong rotation for the outer globular clusters, suggesting a hot rotating halo or an extended bulge system in M31. The role of the halo in M31 has been contentious. Some studies have suggested M31 has an extended bulge but no halo (e.g. Pritchett & van den Bergh 1994; Hurley-Keller et al. 2004; Irwin et al. 2005; Merrett et al.

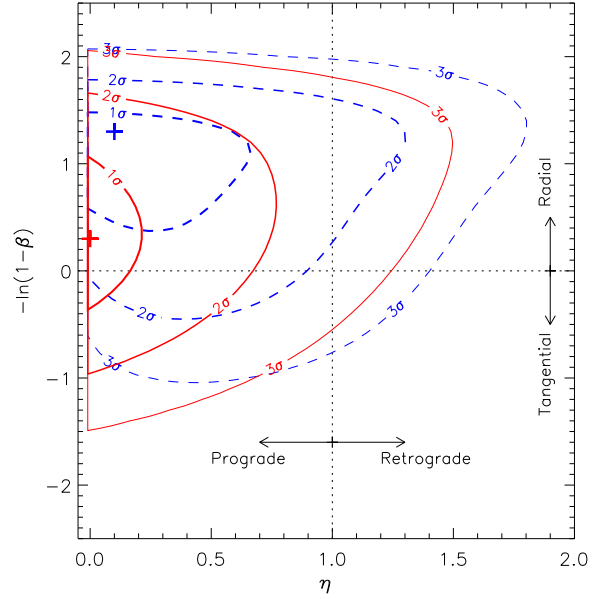


Figure 12. The confidence contours of the orbital parameters η and β for the M31 globular clusters. We only consider globular clusters where $|Y| > 5 \text{ kpc}$ to probe the outer regions and reduce disc contamination. The solid red and dashed blue contours represent the metal-rich ($[\text{Fe}/\text{H}] > -1$) and metal-poor ($[\text{Fe}/\text{H}] < -1$) subsamples respectively

2006), whilst more recent studies have revealed evidence for a huge halo (Chapman et al. 2006; Kalirai et al. 2006; Ibata et al. 2007). The weaker rotational component in the metal-poor sample may suggest a transition from the bulge to a halo component but a larger kinematic sample extending further along the minor-axis is required for confirmation.

6 CONCLUSIONS

We studied the rotational properties of halo populations in the Milky Way Galaxy and Andromeda (M31). We modelled the gravitational potential, Φ , and the density profile of the tracer population, ρ , as spherically symmetric power-laws with indices γ and α respectively. The shape of the velocity distribution is controlled by two parameters, namely β which governs the velocity anisotropy and η which governs the rotation.

For our applications, we used the potential $\Phi \sim r^{-\gamma}$ with $\gamma = 0.5$ as this is a good approximation to a Navarro-Frenk-White profile at large radii. Our tracer populations have a density profile $\rho \sim r^{-\alpha}$ with typically $\alpha = 3.5$. A maximum likelihood method is used to constrain the orbital parameters β and η for five different populations: (1) Milky way halo blue horizontal branch (BHB) stars, (2) Milky Way globular clusters, (3) Milky Way satellites, (4) M31 satellites and (5) M31 globular clusters. We summarise our conclusions as follows:

- (1) From our constructed sample of halo BHB stars from SDSS, we find evidence for two different halo populations: a prograde, rotating, comparatively metal-rich component ($[\text{Fe}/\text{H}] > -2$) and a retrograde, rotating, comparatively metal-poor component ($[\text{Fe}/\text{H}] < -2$). The mean streaming motions are $\langle v_\phi \rangle = (21 \pm 11)(r/10 \text{ kpc})^{-1/4} \text{ kms}^{-1}$ and $\langle v_\phi \rangle = -(35 \pm$

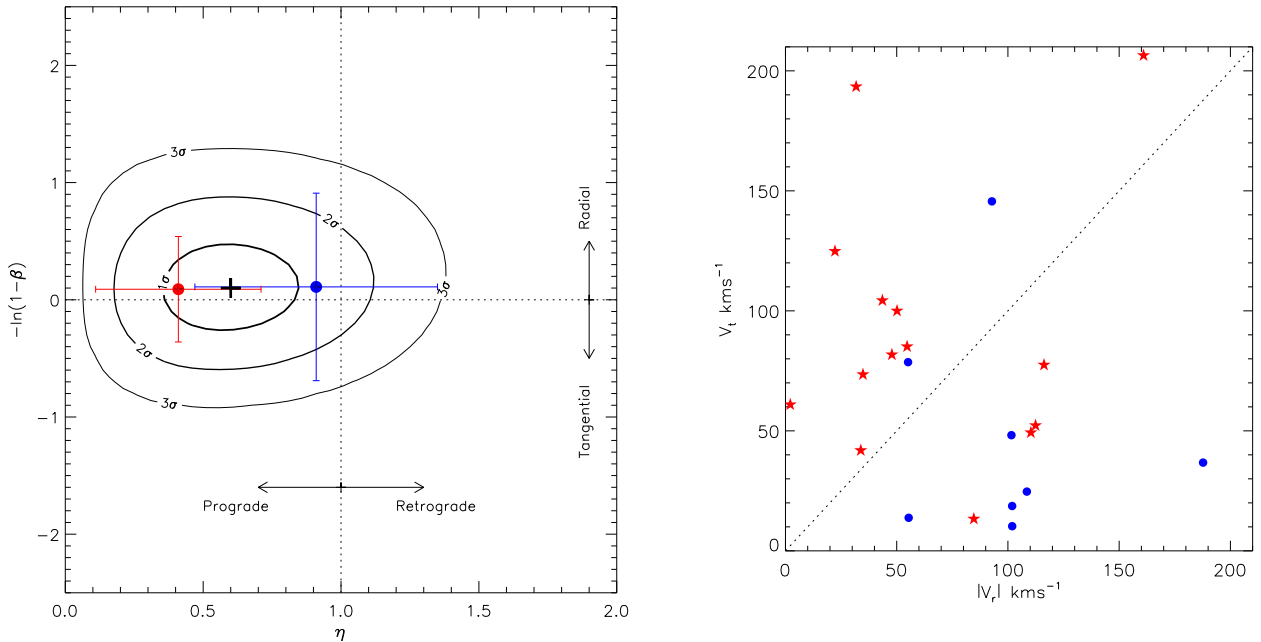


Figure 11. Left: The confidence contours of the orbital parameters η and β for the M31 satellites. The red and blue points correspond to the dSphs (rotating) and non-dSph (non-rotating) subsets respectively. Arrows represent the regions of prograde, retrograde, radial and tangential distributions. Right: The line of sight velocities of the M31 satellites decomposed into tangential and radial components. These are lower limits as only one component of velocity is known. The red stars and blue circles represent the members of the dSph and non-dSph groups respectively.

10) $(r/10 \text{ kpc})^{-1/4} \text{ kms}^{-1}$ for the richer and poorer populations respectively. A rough estimate suggests that these structures may have stellar masses of $M \sim 10^8 M_{\odot}$. We find evidence from the velocity dispersion profile that the metal-rich sample is associated with the accretion of a massive satellite. The line of sight velocity dispersion of the metal-rich sample has a kinematically cold component at $20 < r/\text{kpc} < 30$, which could be evidence for a shell like structure caused by the accretion event. We find no such evidence to suggest the metal-poor sample is associated with an accretion event. We suggest that this population typifies the primordial stellar halo and the net retrograde rotation reflects an underestimate in our adopted local standard of rest circular velocity, which may be as high as $\sim 240 \text{ kms}^{-1}$.

(2) The halo globular clusters of the Milky Way show evidence of net prograde rotation, $\langle v_{\phi} \rangle = (58 \pm 27)(r/10 \text{ kpc})^{-1/4} \text{ kms}^{-1}$, and have a mildly radial velocity distribution. Previous studies have found a mild net prograde rotation from an analysis of the line of sight velocities of the halo globular clusters (e.g. Frenk & White 1980). Our results are in agreement, but this deduction arises from the analysis of those 15 of the 41 halo globular clusters which have available proper motions. We note that the majority of our globular cluster sample have metallicities in the range $-2 < [\text{Fe}/\text{H}] < -1$ and are located between $10 < r/\text{kpc} < 20$. It is interesting that we also see net prograde rotation in the halo BHB stars in this distance and metallicity range. This suggests the relatively metal-rich BHBs and halo globular clusters may share a similar formation history.

(3) Line of sight velocities alone poorly constrain the orbital parameters of the Milky Way satellites. Using available proper motions for 9 of the classical satellites, we find evidence for prograde rotation, $\langle v_{\phi} \rangle = (69 \pm 42)(r/10 \text{ kpc})^{-1/4} \text{ kms}^{-1}$, and a tangential anisotropy parameter $\beta = -1.5^{+0.7}_{-1.0}$. The orbits are preferentially

polar. This leads to the detection of a more pronounced rotation when the normal vector of rotation is inclined by $|\theta| \approx 50^{\circ}$ to the normal of the disc. This hints that the satellites may be part of a rotationally supported disc (as postulated by a number of authors), but without more accurate proper motions this hypothesis cannot be confirmed.

(4) Application of these methods to the M31 satellites is potentially powerful, as the line of sight velocity has contributions from both the tangential and radial velocity components with respect to the M31 centre. The overall population shows hints of prograde rotation. We can divide the satellites into two groups. One possesses pronounced prograde rotation, $\langle v_{\phi} \rangle = (62 \pm 34)(r/10 \text{ kpc})^{-1/4} \text{ kms}^{-1}$, whilst the other shows no evidence for a rotating signal. Interestingly, the rotating group consists entirely of the dwarf spheroidal satellites. The correlation between satellite type and orbital orientation suggests these satellites may share a common origin.

(5) There is a rich dataset on the M31 globular clusters which remains relatively unexploited. We examined the globular clusters with projected distance along the minor-axis greater than 5 kpc. These outer globular clusters have prograde rotation which is more pronounced for the metal-rich ($[\text{Fe}/\text{H}] > -1$) subset. We find $\langle v_{\phi} \rangle = (94 \pm 35)(r/10 \text{ kpc})^{-1/4} \text{ kms}^{-1}$ for the metal-rich population and $\langle v_{\phi} \rangle = (53 \pm 34)(r/10 \text{ kpc})^{-1/4} \text{ kms}^{-1}$ for the metal-poor population. The strong rotation, especially in the metal-rich sample, suggests these globular clusters may belong to the M31 bulge system. However, a more robust explanation awaits a more substantial kinematic sample extending further along the minor-axis.

The *Gaia* satellite promises to provide proper motion data on all

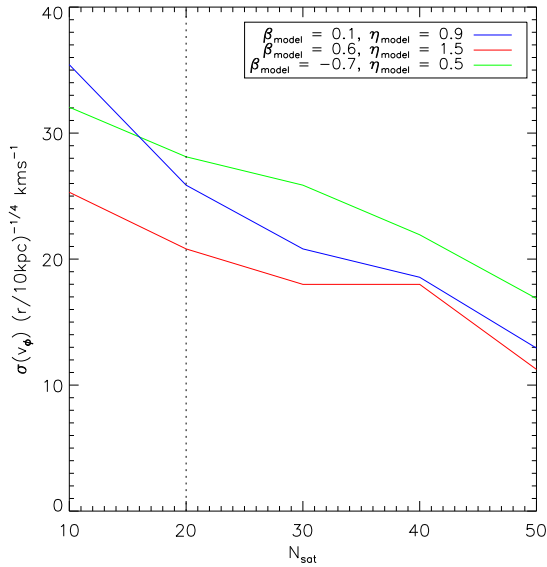


Figure 13. The estimated error in the mean streaming motion of the Milky Way satellites as a function of number of satellites. We assume random errors on the tangential velocity components in the range $1 \text{ km s}^{-1} \leq \sigma \leq 15 \text{ km s}^{-1}$. Three different models are used, shown by the blue ($\eta = 0.9$, $\beta = 0.1$), red ($\eta = 1.9$, $\beta = 0.6$) and green ($\eta = 0.5$, $\beta = -0.7$) lines respectively.

dwarf galaxies of the Milky Way and M31 and for thousands of halo stars. Wilkinson & Evans (1999) suggested that *Gaia* can constrain the proper motion of distant classical dwarfs in the Milky way, like Leo I, to within $\pm 15 \text{ km s}^{-1}$ and nearer dwarfs like Ursa Minor to within $\pm 1 \text{ km s}^{-1}$. Whilst *Gaia* will improve the proper motion measurements for the classical satellites, deeper complements to *Gaia* such as the LSST will be needed to achieve this level of accuracy for the ultra-faint satellites.

In anticipation of this future work, we close by considering Monte Carlo simulations of our distribution functions to estimate how well we can constrain rotation with these future astrometric surveys. We assume random errors on the tangential velocity components between 1 km s^{-1} and 15 km s^{-1} . Fig. 13 gives a rough estimate of how the accuracy depends on the number of satellites with proper motion measurements. For $N \approx 20$ satellites, we can constrain the mean streaming motion to $\sigma_{v_\phi} \approx 30(r/10 \text{ kpc})^{-1/4} \text{ km s}^{-1}$. This evaluates to $\sigma_{v_\phi} \approx (10 - 20) \text{ km s}^{-1}$ for satellites between $r = (50 - 250) \text{ kpc}$. The combination of more accurate proper motion measurements with radial velocities can potentially probe any apparent kinematic dichotomy between the classical and ultra-faint satellites, and perhaps provide more robust evidence bearing on the disc of satellites.

Our analysis of the Milky Way stellar halo using BHB stars will be greatly improved by increasing the number of targets at larger radii. Coupled with more accurate radial velocity measurements, we will be able to map the kinematic structure of the stellar halo in greater detail and see if the apparent dual nature of the metal-rich and metal-poor components continues out to further reaches of the halo. LSST will hopefully play a vital role in finding these BHB targets.

ACKNOWLEDGEMENTS

We thank the anonymous referee for a thorough reading of this manuscript and for very useful comments. AJD thanks the Science and Technology Facilities Council (STFC) for the award of a studentship, whilst VB acknowledges financial support from the Royal Society.

REFERENCES

- Abadi M. G., Navarro J. F., Steinmetz M., 2006, *MNRAS*, 365, 747
- An D., et al., 2008, *ApJS*, 179, 326
- Battaglia G., et al., 2005, *MNRAS*, 364, 433
- Bell E. F., et al., 2008, *ApJ*, 680, 295
- Belokurov V., et al., 2008, *ApJ*, 686, L83
- Belokurov V., et al., 2009, *MNRAS*, 397, 1748
- Binney J., Tremaine S., 1987, *Galactic dynamics*. Princeton, NJ, Princeton University Press, 1987, 747 p.
- Bovy J., Hogg D. W., Rix H., 2009, *ApJ*, 704, 1704
- Caldwell N., Harding P., Morrison H., Rose J. A., Schiavon R., Kriessler J., 2009, *AJ*, 137, 94
- Carney B. W., Laird J. B., Latham D. W., Aguilar L. A., 1996, *AJ*, 112, 668
- Carollo D., et al., 2007, *Nature*, 450, 1020
- Casetti-Dinescu D. I., Girard T. M., Herrera D., van Altena W. F., López C. E., Castillo D. J., 2007, *AJ*, 134, 195
- Chapman S. C., Ibata R., Lewis G. F., Ferguson A. M. N., Irwin M., McConnachie A., Tanvir N., 2006, *ApJ*, 653, 255
- Chiba M., Beers T. C., 2000, *AJ*, 119, 2843
- Collins M. L. M., et al., 2009, *ArXiv e-prints*
- Cotton W. D., Condon J. J., Arbizzani E., 1999, *ApJS*, 125, 409
- Crampton D., Cowley A. P., Schade D., Chayer P., 1985, *ApJ*, 288, 494
- de Vaucouleurs G., 1958, *ApJ*, 128, 465
- Diemand J., Kuhlen M., Madau P., 2007, *ApJ*, 667, 859
- Dinescu D. I., Girard T. M., van Altena W. F., 1999, *AJ*, 117, 1792
- Dinescu D. I., Girard T. M., van Altena W. F., López C. E., 2005, *ApJ*, 618, L25
- Djorgovski S., Meylan G., 1994, *AJ*, 108, 1292
- Eggen O. J., Lynden-Bell D., Sandage A. R., 1962, *ApJ*, 136, 748
- Evans N. W., de Zeeuw P. T., 1994, *MNRAS*, 271, 202
- Evans N. W., Hafner R. M., de Zeeuw P. T., 1997, *MNRAS*, 286, 315
- Evans N. W., Wilkinson M. I., 2000, *MNRAS*, 316, 929
- Evans N. W., Wilkinson M. I., 2001, in J. W. Menzies & P. D. Sackett ed., *Microensing 2000: A New Era of Microensing Astrophysics* Vol. 239 of *Astronomical Society of the Pacific Conference Series*, *The Haloes of the Milky Way and Andromeda Galaxies*. pp 299–+
- Freeman K. C., 1987, *ARA&A*, 25, 603
- Frenk C. S., White S. D. M., 1980, *MNRAS*, 193, 295
- Galleti S., Bellazzini M., Federici L., Buzzoni A., Fusi Pecci F., 2007, *A&A*, 471, 127
- Galleti S., Federici L., Bellazzini M., Fusi Pecci F., Macrina S., 2004, *A&A*, 416, 917
- Geha M., Willman B., Simon J. D., Strigari L. E., Kirby E. N., Law D. R., Strader J., 2009, *ApJ*, 692, 1464
- Harris W. E., 1976, *AJ*, 81, 1095
- Harris W. E., 1996, *VizieR Online Data Catalog*, 7195, 0
- Hartwick F. D. A., 1983, *Memorie della Societa Astronomica Italiana*, 54, 51

- Hartwick F. D. A., 1987, in G. Gilmore & B. Carswell ed., NATO ASIC Proc. 207: The Galaxy The structure of the Galactic halo. pp 281–290
- Hurley-Keller D., Morrison H. L., Harding P., Jacoby G. H., 2004, *ApJ*, 616, 804
- Ibata R., Martin N. F., Irwin M., Chapman S., Ferguson A. M. N., Lewis G. F., McConnachie A. W., 2007, *ApJ*, 671, 1591
- Irwin M. J., Ferguson A. M. N., Ibata R. A., Lewis G. F., Tanvir N. R., 2005, *ApJ*, 628, L105
- Ivezic Z., Tyson J. A., Allsman R., Andrew J., Angel R., for the LSST Collaboration 2008, ArXiv e-prints
- Kalirai J. S., et al., 2006, *ApJ*, 648, 389
- Kalirai J. S., et al., 2009, *ApJ*, 705, 1043
- Karachentsev I. D., Karachentseva V. E., Huchtmeier W. K., Makarov D. I., 2004, *AJ*, 127, 2031
- Kim S. C., et al., 2007, *AJ*, 134, 706
- Kinman T. D., Cacciari C., Bragaglia A., Buzzoni A., Spagna A., 2007, *MNRAS*, 375, 1381
- Kinman T. D., Suntzeff N. B., Kraft R. P., 1994, *AJ*, 108, 1722
- Klypin A., Zhao H., Somerville R. S., 2002, *ApJ*, 573, 597
- Koch A., et al., 2009, *ApJ*, 690, 453
- Koposov S. E., Rix H., Hogg D. W., 2010, *ApJ*, 712, 260
- Kroupa P., Theis C., Boily C. M., 2005, *A&A*, 431, 517
- Lee M. G., Hwang H. S., Kim S. C., Park H. S., Geisler D., Sarajedini A., Harris W. E., 2008, *ApJ*, 674, 886
- Letarte B., et al., 2009, *MNRAS*, 400, 1472
- Libeskind N. I., Frenk C. S., Cole S., Jenkins A., Helly J. C., 2009, *MNRAS*, 399, 550
- Lynden-Bell D., 1983, in E. Athanassoula ed., Internal Kinematics and Dynamics of Galaxies Vol. 100 of IAU Symposium, The origin of dwarf spheroidal galaxies. pp 89–91
- Majewski S. R., 1992, *ApJS*, 78, 87
- Majewski S. R., et al., 2007, *ApJ*, 670, L9
- Martin N. F., Ibata R. A., Chapman S. C., Irwin M., Lewis G. F., 2007, *MNRAS*, 380, 281
- Mateo M. L., 1998, *ARA&A*, 36, 435
- McConnachie A. W., Irwin M. J., 2006, *MNRAS*, 365, 902
- Méndez R. A., Platais I., Girard T. M., Kozhurina-Platais V., van Altena W. F., 1999, *ApJ*, 524, L39
- Merrett H. R., et al., 2006, *MNRAS*, 369, 120
- Metz M., Kroupa P., Jerjen H., 2007, *MNRAS*, 374, 1125
- Metz M., Kroupa P., Libeskind N. I., 2008, *ApJ*, 680, 287
- Miceli A., et al., 2008, *ApJ*, 678, 865
- Navarro J. F., Frenk C. S., White S. D. M., 1996, *ApJ*, 462, 563
- Newberg H. J., Sloan Digital Sky Survey Collaboration 2003, in Bulletin of the American Astronomical Society Vol. 35 of Bulletin of the American Astronomical Society, Sloan Extension for Galactic Underpinnings and Evolution (SEGUE). pp 1385–
- Norris J., 1986, *ApJS*, 61, 667
- Norris J. E., Ryan S. G., 1989, *ApJ*, 336, L17
- Olling R. P., Merrifield M. R., 1998, *MNRAS*, 297, 943
- Palma C., Majewski S. R., Johnston K. V., 2002, *ApJ*, 564, 736
- Perrett K. M., Bridges T. J., Hanes D. A., Irwin M. J., Brodie J. P., Carter D., Huchra J. P., Watson F. G., 2002, *AJ*, 123, 2490
- Piatek S., Pryor C., Bristow P., Olszewski E. W., Harris H. C., Mateo M., Minniti D., Tinney C. G., 2005, *AJ*, 130, 95
- Piatek S., Pryor C., Bristow P., Olszewski E. W., Harris H. C., Mateo M., Minniti D., Tinney C. G., 2006, *AJ*, 131, 1445
- Piatek S., Pryor C., Bristow P., Olszewski E. W., Harris H. C., Mateo M., Minniti D., Tinney C. G., 2007, *AJ*, 133, 818
- Piatek S., Pryor C., Olszewski E., 2008a, Space Motions of the Draco, Fornax, and Sagittarius Dwarf Spheroidal Galaxies. Korbalski, B. S. & Jerjen, H., pp 199–
- Piatek S., Pryor C., Olszewski E. W., 2008b, *AJ*, 135, 1024
- Piatek S., Pryor C., Olszewski E. W., Harris H. C., Mateo M., Minniti D., Tinney C. G., 2003, *AJ*, 126, 2346
- Pritchett C. J., van den Bergh S., 1994, *AJ*, 107, 1730
- Quinn P. J., Goodman J., 1986, *ApJ*, 309, 472
- Ratnatunga K. U., Freeman K. C., 1985, *ApJ*, 291, 260
- Reid M. J., et al., 2009, *ApJ*, 700, 137
- Sales L. V., Navarro J. F., Abadi M. G., Steinmetz M., 2007, *MNRAS*, 379, 1464
- Schönrich R., Binney J., Dehnen W., 2010, *MNRAS*, pp 149–
- Simon J. D., Geha M., 2007, *ApJ*, 670, 313
- Sirko E., et al., 2004a, *AJ*, 127, 899
- Sirko E., et al., 2004b, *AJ*, 127, 914
- Smith M. C., et al., 2007, *MNRAS*, 379, 755
- Sommer-Larsen J., Beers T. C., Flynn C., Wilhelm R., Christensen P. R., 1997, *ApJ*, 481, 775
- Turon C., O’Flaherty K. S., Perryman M. A. C., eds, 2005, The Three-Dimensional Universe with Gaia Vol. 576 of ESA Special Publication
- Walker M. G., Mateo M., Olszewski E. W., 2008, *ApJ*, 688, L75
- Watkins L. L., et al., 2009, *MNRAS*, 398, 1757
- Watkins L. L., Evans N. W., An J., 2010, ArXiv e-prints
- Wilhelm R., Beers T. C., Gray R. O., 1999, *AJ*, 117, 2308
- Wilhelm R., Beers T. C., Kriessler J. R., Pier J. R., Sommer-Larsen J., Layden A. C., 1996, in H. L. Morrison & A. Sarajedini ed., Formation of the Galactic Halo...Inside and Out Vol. 92 of Astronomical Society of the Pacific Conference Series, Halo Kinematics from the Field Horizontal Branch Stars. pp 171–
- Wilkinson M. I., Evans N. W., 1999, *MNRAS*, 310, 645
- Woolley R., 1978, *MNRAS*, 184, 311
- Xue X. X., et al., 2008, *ApJ*, 684, 1143
- Yanny B., et al., 2000, *ApJ*, 540, 825
- York D. G., et al., 2000, *AJ*, 120, 1579
- Zaritsky D., Gonzalez A. H., 1999, *PASP*, 111, 1508
- Zinn R., 1985, *ApJ*, 293, 424
- Zucker D. B., et al 2007, *ApJ*, 659, L21